Photodisintegration cross section of ^{4}He in the giant dipole resonance energy region

M. Murata,[1] T. Kawabata,[2] S. Adachi,[3] H. Akimune,[4] S. Amano,[5] Y. Fujikawa,[6] T. Furuno,[2]
K. Inaba,[6] Y. Ishii,[6] S. Miyamoto,[5,7] M. Tsumura,[6] and H. Utsunomiya[4,8]

[1]*Research Center for Nuclear Physics (RCNP), Osaka University, Ibaraki, Osaka 567-0047, Japan*
[2]*Department of Physics, Osaka University, Toyonaka, Osaka 560-0043, Japan*
[3]*Cyclotron and Radioisotope Center (CYRIC), Tohoku University, Sendai, Miyagi 980-8578, Japan*
[4]*Faculty of Science and Engineering, Konan University, Kobe, Hyogo 658-8501, Japan*
[5]*Laboratory of Advanced Science and Technology for Industry (LASTI), University of Hyogo, Ako, Hyogo 678-1205, Japan*
[6]*Department of Physics, Kyoto University, Sakyo, Kyoto 606-8502, Japan*
[7]*Institute of Laser Engeneering, Osaka University, Suita, Osaka 565-0871, Japan*
[8]*Shanghai Advanced Research Institute, Chinese Academy of Science, Shanghai 201210, China*

We simultaneously measured the ^{4}He$(\gamma, n)\,^3$He and ^{4}He$(\gamma, p)\,^3$H reactions in the energy range around the giant dipole resonance. A quasi-monoenergetic photon beam produced via the laser Compton scattering technique was irradiated on the active-target time-projection chamber filled with helium gas, and trajectories of charged decay particles emitted from ^{4}He were measured. Our data suggest that the ^{4}He$(\gamma, n)\,^3$He and ^{4}He$(\gamma, p)\,^3$H cross sections peak around 26 MeV. This result contradicts the previous experimental data reported by Shima *et al.* [Phys. Rev. C **72**, 044004 (2005)] but is consistent with other experimental results.

I. INTRODUCTION

The isovector giant dipole resonance (GDR) is one of the most examined nuclear resonances, which is excited through the $E1$ transition of nuclear ground states. It is a representative example of the collective excitation modes of atomic nuclei in which protons and neutrons coherently oscillate in antiphase, and its energy-integrated cross section exhausts approximately 100% of the Thomas-Reiche-Kuhn sum-rule value [1]. The photodisintegration reaction is a suitable probe to investigate the GDR because the photoabsorption dominantly induces $E1$ transition as the long wave-length approximation commonly holds in various nuclei.

The cross section of the ^{4}He photodisintegration reaction in the GDR energy region has recently attracted research interest because it is an important aspect for understanding the nucleosynthesis process in the universe. One example is the ν process in the He layer of core-collapse supernovae [2]. In this process, rare elements such as ^{7}Li and ^{11}B are produced through a series of nuclear reactions initiated by the ^{4}He$(\nu, \nu'n)$ and ^{4}He$(\nu, \nu'p)$ reactions [3]. The giant resonances, such as GDR and spin-dipole resonances, make a dominant contribution on these reactions because the ^{4}He(ν, ν') reaction primarily excites these resonances with $L = 1$ [4]. The Gamow-Teller resonance is approximately forbidden in ^{4}He due to the system's double magicity. Because of technical difficulties in measuring neutrino-nucleus reactions, estimation of neutrino-nucleus reaction cross sections for examining the ν process relies on the nuclear structure theories. Nuclear structural information is therefore a source of uncertainty with regard to the calculations. By using the analogy

between electromagnetic responses and weak responses of nuclei [5], the experimental cross sections of the ^{4}He photodisintegration reaction can provide a criterion to test the validity of the estimated neutrino-nucleus reactions cross sections.

Furthermore, a relationship was also discussed between the ^{4}He photodisintegration and the lithium problem in the big bang nucleosynthesis (BBN) [6]. The lithium problem is an unsolved discrepancy between the primordial abundances of lithium isotopes estimated from the astronomical observation and those predicted from the BBN calculation. It is an intriguing problem that the primordial abundance of ^{7}Li estimated from observing the metal-poor halo starts is deficient with regard to the standard BBN prediction by a factor of three [7,8]. In addition, the possibility of an overabundance of ^{6}Li at the level of approximately three orders of magnitude was also suggested from the spectroscopic measurements [9]. It was proposed that the extended BBN modified with nonthermal photons produced through radiative decays of unstable relic neutral massive particles might solve the lithium problem [6]. Although the relic particle has not yet been observed, its possible mass, abundance, and lifetime are constrained by the cross sections of the ^{4}He photodisintegration reaction.

The experimental studies on the ^{4}He photodisintegration reaction have continuously been reported since the 1950s [10–37]. Most of the previous studies measured one of the (γ, n) and (γ, p) reactions and fewer studies were conducted using the simultaneous measurement [10,11,15,21,22,27,32,35–37]. Some authors measured the photodisintegration reactions directly [10,11,14,15,17–23,27, 30,32,33,35–37], while others deduced its cross section from

the surrogate reactions, such as the radiative capture reactions, which is the inverse reaction of the photodisintegration reactions [12,13,16,24–26,28,29,31,34]. Although the direct measurements in early years were conducted with continuous-energy photon beams generated with bremsstrahlung, the quasi-monoenergetic beam generated from the laser Compton scattering (LCS) [27,32,35–37] or tagged photon technique [33] were employed in the recent measurement.

However, these previous results exhibit significant deviation beyond their respective error ranges. Therefore, it is difficult to extract reliable information to constrain theoretical calculations. Here, we focused on the recent experimental studies [32,35–37] in which quasi-monoenergetic photon beams were employed, and both the (γ, n) and (γ, p) channels were simultaneously measured. Regarding the reaction probe, quasi-monoenergetic photon beams are more suitable than continuous-energy beams since the unfolding procedure is necessary for the continuous-energy beams. This unfolding process could cause significant errors on the cross sections, unless the stability of the accelerator, sufficient counting statistics, and understanding of the beam-energy spectrum were guaranteed. Furthermore, the simultaneous measurement is desirable to obtain reliable cross sections of the (γ, n) and (γ, p) reactions because one can cancel out the experimental errors due to the target thickness and the beam flux.

Firstly, Shima *et al.* [32] performed the measurement using a time-projection chamber (TPC). By operating the TPC as an active target, they measured the trajectories of charged particles and their energy deposits along the trajectories. Their deliberate experimental design and careful treatments of the data made it possible to clearly distinguish photodisintegration events from background events. They reported that no peak structures were observed in the photon-energy dependence of the cross sections of the (γ, n) and (γ, p) reactions at $E_\gamma < 30$ MeV. A follow-up measurement by Shima *et al.* presented a preliminary result suggesting that the peak of the GDR is located around $E_\gamma = 32$ MeV [35].

Raut *et al.* [37] and Tornow *et al.* [36] carried out the measurement in the HIγS facility using a high-pressure ^{4}He-Xe gas scintillator as an active target. They identified photodisintegration events of ^{4}He by measuring the total energy deposit of decay charged particles in the detector. The thick target and intense beam allowed them to obtain statistically high precision data. The theoretical calculations [38] describe the measured cross sections reasonably well and suggest that the peak of the GDR is located around $E_\gamma = 26$ MeV. However, they did not report the cross sections of the (γ, n) reactions in the lower energy region of $E_\gamma < 27$ MeV. Thus, we cannot conclude the energy dependence of the cross sections of the (γ, n) and (γ, p) channels solely from their result.

From a theoretical perspective, an elaborate calculation using a realistic nuclear force with a three-body interaction was reported [39]. The cross sections of the ^{4}He$(\gamma, n)^3$He and the ^{4}He$(\gamma, p)^3$H reactions were calculated in the microscopic R-matrix approach, in which final state interactions and two- and three-body decay channels were considered. Both theoretical cross sections of the (γ, n) and (γ, p) reactions rise sharply from the threshold and become maximal at $E_\gamma = 26$ MeV. This result is consistent with the cross sections previously
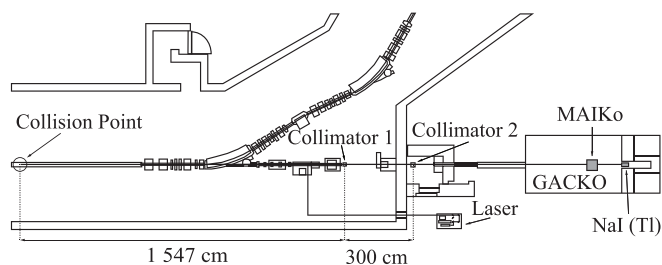

FIG. 1. Top view of the BL01 at the NewSUBARU synchrotron radiation facility. Infrared photon beams generated with the Nd:YVO$_4$ laser modules were guided into the electron storage ring after two reflections. The back-scattered photons resulting from the head-on collision with relativistic electrons coming from the left were guided straight to the GACKO beam hutch. The MAIKo active target and the NaI(Tl) beam monitor were installed in the GACKO beam hutch. On the way to the hutch, photons were sieved with the two collimators to be quasi-monoenergetic photon beams.

calculated using the Lorentz integral transform method [38] and discrepant with the results by Shima *et al.*

The data from Shima *et al.* contradicts most of previous experimental data and theoretical calculations, and thus, the results appear unfavorable. However, their measurements using an active target TPC to track the charged particle trajectories in the final state are unprecedentedly sophisticated. Background events could be effectively rejected with information from the particle trajectories. Therefore, the possibility that their results differing from the other experiments are correct cannot be ruled out owing to their improved methodology. In order to solve this situation, we simultaneously measured the cross sections of the ^{4}He$(\gamma, n)^3$He and ^{4}He$(\gamma, p)^3$H reactions using one experimental setup with a new active target TPC for elucidating the energy dependence of the cross sections in the GDR region. In this paper, we report the cross sections of the ^{4}He$(\gamma, n)^3$He and ^{4}He$(\gamma, p)^3$H reactions in the energy region between $E_\gamma = 23$–30 MeV measured using a quasi-monoenergetic photon beams generated with the LCS technique and the active target TPC.

II. EXPERIMENT

The experiment was performed at the beam line 01 (BL01) [40] in the NewSUBARU synchrotron radiation facility. Figure 1 shows an overview of the experimental setup. A quasi-monoenergetic γ-ray beam with a maximum energy of $E_\gamma = 23$–30 MeV was produced using the LCS technique. Laser photons generated using the solid-state laser (Nd:YVO$_4$ $\lambda = 1064$ nm) were injected into the storage ring at NewSUBARU and impinged on the electron beam circulating in it. The energy of the laser photon was amplified through Compton scattering with a high-energy electron. The resultant energy was determined from its scattering angle and the energy of the electron beam. Photons scattered at $180°$, which had the highest energy, were selected by limiting the scattering angle with the lead collimators installed on the BL01. A pair of collimators was located at 1547 and 1848 cm
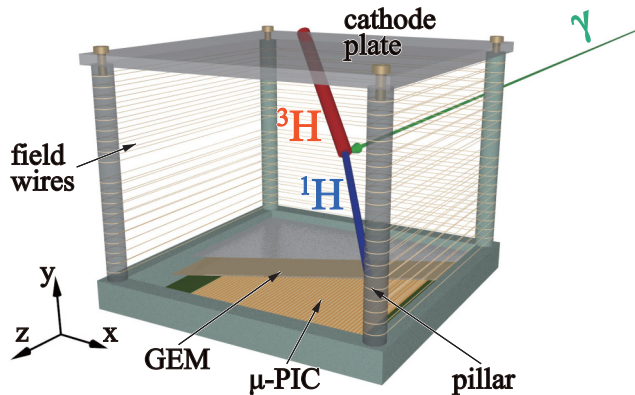
FIG. 2. Schematic picture of the MAIKo active target. This figure displays a typical ^{4}He$(\gamma, p)^3$H event, in which a ^{4}He nucleus absorbs a photon (thin green arrow emanating from behind the MAIKo active target) to break up into a ^{3}H nucleus (the thickest red line) and a proton (thicker blue line). Electrons generated along the trajectories of the decay particles were drifted with the uniform electric field to the μ-PIC at the bottom. For good visibility, field wires on the front side and the lower half of the GEM are not drawn.

TABLE I. Summary of the pressure and effective thickness of the detection gas. k is the index of the beam energy. E_e and $E_{\max}$ stand for the energy of the electron beam and the maximum energy of the γ-ray beam, respectively. Effective thickness is a mass thickness at the depth of the sensitive volume (10 cm).

k	E_e (GeV)	$E_{\max}$ (MeV)	Pressure (hPa)	Thickness (mg/cm^2)
1	1.146	23.0	500	1.05
2	1.171	24.0	500	1.05
3	1.195	25.0	1000	2.09
4	1.243	27.0	1000	2.09
5	1.266	28.0	1000	2.09
6	1.311	30.0	2000	4.18

away from the collision point, and their apertures were 3 mm and 2 mm, respectively.

The energy of the γ-ray beam was tunable by altering the energy of the electron beam, and its absolute value was precisely calibrated [41]. For this experiment, an electron beam with an energy of 1 GeV delivered from the injector linear accelerator was accelerated to 1.146–1.311 GeV in the storage ring.

A linearly polarized γ-ray beam was employed in the present measurement. The laser photons were almost 100% linearly polarized, and a half-wave plate was used to tilt the polarization axis of the laser photons at 10° from the horizontal axis. Because the polarization of the LCS γ rays is maximum at the scattering angle of 180° [42], highly polarized beams were obtained at the GACKO beam hutch.

The γ-ray beam was monitored with the NaI(Tl) scintillation detector installed at the end of the BL01. A crystal of the NaI(Tl) scintillator was cut into a cylindrical shape with a diameter of 203.2 mm (8 in.) and a thickness of 304.8 mm (12 in.). The γ-ray beam provided through the collimator of the finite-size aperture inevitably had an energy spread as the energy of the scattered photon correlates to the Compton scattering angle. In order to estimate the total photon number irradiated on the target, the energy spectra deposited to the NaI(Tl) scintillator by the LCS photon beams were acquired during the measurement. In addition, the energy spectrum with a low-intensity beam was also measured at each beam energy to deduce the energy profile.

Charged particles emitted from the photodisintegration of ^{4}He were measured using the MAIKo active target [43]. As shown in Fig. 1, the MAIKo active target was installed in the GACKO beam hutch on the BL01. A schematic view of the MAIKo active target is shown in Fig. 2. The MAIKo active target worked as a TPC. A negative high voltage was applied on the cathode plate at the top of the MAIKo to form

a vertical electric field. Field wires made of beryllium copper were doubly wound around the pillars with 5-mm intervals to form a uniform electric field. The sensitive volume of the TPC was the cubic region enclosed in the field cage. Its dimension defined with the area of the read-out electrodes, and the field cage was $10 \times 10 \times 11$ cm^3 in width, depth, and height, respectively. The field cage was aligned so that one dimension of it was normal to the beam direction. As shown in Fig. 2, hereinafter we define the three-dimensional Cartesian coordinates such that the z axis is parallel to the beam direction and the y axis is vertical.

The whole structure shown in Fig. 2 was installed in the vacuum chamber filled with the detection gas. The detection gas comprised helium with 90% and CH$_4$ with 10% by their partial pressures, in which helium and CH$_4$ served as the target and quench gas, respectively. The gas pressure was optimized to realize the condition that the ranges of the proton and ^{3}H were long enough to escape from the sensitive volume, whereas that of ^{3}He was short enough to stop inside the sensitive volume, as summarized in Table I.

As an incident γ ray was absorbed by a ^{4}He nucleus inside the sensitive volume, the ^{4}He nucleus decayed into a proton and a ^{3}H nucleus (a neutron and a ^{3}He nucleus), which traveled in the opposite directions. Those charged decay particles ionized gas molecules along their trajectories and kicked out electrons. These electrons were drifted toward the negative direction of the y axis by the uniform electric field inside the drift cage and gas-amplified by the gas electron multiplier (GEM). Finally, the amplified electrons reached the micropixel chamber (μ-PIC) [44] at the bottom of the MAIKo active target. The μ-PIC consisted of 400-μm pitched 256×256 circular pixels aligned in the square region. Each pixel was composed of a cylindrical anode electrode with a diameter of 50 μm at the center and a cathode electrode on the circumference with a diameter of 256 μm. The electrons reached the pixels, caused a Townsend avalanche in the high electric field formed around the anode electrodes, and induced electric signals on the anode and cathode electrodes. The anode (cathode) electrodes on the pixels in line were electrically connected to form 256 anode (cathode) strips for signal readout.
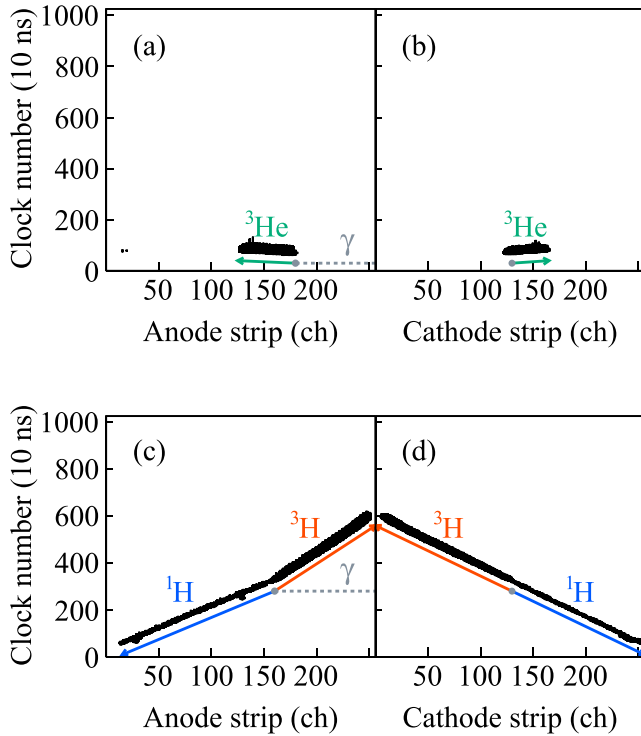
FIG. 3. Typical track images measured with the MAIKo active target. (a) and (b) present a ^{4}He$(\gamma, n)\,^3$He event, and (c) and (d) indicate a ^{4}He$(\gamma, p)\,^3$H event.

The electric signals induced on the μ-PIC were read out and processed with the dedicated electronics with the amplifier-shaper-discriminator (ASD) [45]. When a trigger signal was provided to the signal readout electronics, the status of the discriminators at every 10 ns (100 MHz) was recorded as a function of the clock number within a time window of 10.24 μs. Thus, the acquired data were equivalent to two black-and-white images with 256×1024 pixels in which the time-over-threshold of the signal was presented with the filled pixels, as shown in Fig. 3. The clock number corresponds to the vertical position from where the trigger event occurred. In contrast, the strip number is the horizontal position. Because the directions of the cathode strips were parallel to the z axis, and those of the anode strips were parallel to the x axis, the black-and-white image obtained from the anode (cathode) strips presented particle trajectories projected onto the xy (zy) plane. Figures 3(a) and 3(b) show two-dimensional images of a typical ^{4}He$(\gamma, n)\,^3$He event, whereas Figs. 3(c) and 3(d) are those of a typical ^{4}He$(\gamma, p)\,^3$H event. ^{3}He was observed as one thick trajectory, and proton and ^{3}H left two thin and medium long trajectories. All trajectories of charged particles started from the horizontal center of cathode images, where the beam-injection point was located. By combining a couple of images, we could reconstruct the three-dimensional configuration of the charged particle trajectories.

Analog signals on adjacent 32 consecutive strips were summed up, and the waveform of the summed signal was also sampled at a frequency of 25 MHz. Because the time constant of the shaping amplifiers was shorter than the typical time

scale of the induced signal, one could obtain energy-deposit information by integrating the waveform. The summed signals were also employed for the trigger decision.

The trigger signal was generated when the pulse height of any summed signals exceeded the threshold level. The threshold level was set sufficiently low so as to avoid missing the photodisintegration events. The trigger rate was less than 100 Hz, and the data acquisition efficiency was higher than 99%.

III. ANALYSIS

A. Event selection

First, candidates of the ^{4}He photodisintegration events were selected out of all the events acquired with the MAIKo active target. The main sources of background events were electrons emitted from Compton scattering and discharges that occurred on the μ-PIC. Photodisintegration events of ^{12}C in CH$_4$ molecules were also a source of the background. Another source would be the photodisintegration events occurring outside the sensitive volume. The shapes of the analog signals resulting from the Compton scattering events and the discharging events were distinctively different from those of the photodisintegration events. Furthermore, the photodisintegration events that arose outside the sensitive volume did not produce any signals significantly higher than the noise level on the μ-PIC electrodes adjacent to the beam axis. Thus, these background events were safely excluded using the pulse-shape information. These event selection criteria were set loose enough so as not to exclude the ^{4}He photodisintegration events. After this selection procedure, the number of events was reduced by one order of magnitude.

Second, we performed tracking analysis to extract the ^{4}He$(\gamma, n)\,^3$He and ^{4}He$(\gamma, p)\,^3$H events from the candidate events selected by the pulse-shape analysis. The ^{4}He$(\gamma, n)\,^3$He events exhibited one short thick trajectory due to ^{3}He, which terminated inside the sensitive volume. On the other hand, the ^{4}He$(\gamma, p)\,^3$H events left two long thin and medium trajectories due to a proton and a ^{3}H nucleus which continued to the boundary of the sensitive volume.

The procedure of the tracking analysis was as follows. Following the cartesian coordinate defined in Fig. 2, we refer to the track image obtained from the anode (cathode) strips as ZY (XY) image hereafter.

(1) Clear false hit pixels due to electric noise in the ZY and XY images.
(2) Determine the reaction point in the XY image. The x position of the reaction point was fixed at the center of the beam axis, and the y position was determined by averaging the y positions of the hits around the beam axis.
(3) Track the trajectories starting from the reaction point in the XY image and derive the number, direction, and length of the trajectories.
(4) By using the y position of the reaction point in the XY image, determine the reaction point in the ZY image, and track the trajectories in the ZY image.

(5) Based on the y positions of the end points in the XY and ZY images, determine the combination of the trajectories in the two images to reconstruct the three-dimensional trajectories.

After the tracking analysis, the analyzed events were classified with the number of reconstructed trajectories. When only one trajectory was reconstructed, this event was classified as a candidate of the ^{4}He(γ, n) ^{3}He event. If two trajectories were reconstructed, this event was classified as a candidate of the ^{4}He(γ, p) ^{3}H event. For further analysis, we calculated total energy loss in the sensitive volume (E) and the differential energy loss (dE/dx) of the reconstructed trajectory. We utilized them to reject the remaining background due to the ^{12}C photodisintegration.

For the ^{4}He(γ, n) ^{3}He candidates, we required the five conditions below.

(i) The number of reconstructed trajectories is one.
(ii) The reaction point is at least 1 cm distant from the edge of the sensitive volume.
(iii) The end point of the trajectory is inside the sensitive volume.
(iv) The correlation between E and the trajectory length is consistent with that of ^{3}He.
(v) Kinematically reconstructed beam energy is in the range between $E_{\max} - 1$ and $E_{\max}$ MeV.

For the ^{4}He(γ, p) ^{3}H candidates, we imposed five conditions below.

(i) The number of reconstructed trajectories is two.
(ii) The reaction point is at least 1 cm distant from the edge of the sensitive volume.
(iii) The two trajectories reach the edge of the sensitive volume.
(iv) dE/dx of one trajectory is consistent with that of a proton, and dE/dx of the other trajectory is consistent with that of ^{3}H.
(v) The two trajectories are oriented in a back-to-back direction in the XY image.

Finally, we defined events that satisfy the above conditions the procedure as true photodisintegration events. Because there should be some true events lost in the tracking and event-selection procedures, it was necessary to consider the detection efficiency of the true events with the MAIKo active target to determine the cross sections.

B. Efficiency estimation

The detection efficiency with the MAIKo active target was estimated using a Monte Carlo simulation. We generated photodisintegration events inside the sensitive volume of the MAIKo active target and simulated various process such as ionization of the detection gas by decay particles, transport process of electrons, gas amplification on the GEM and μ-PIC, and response of the readout circuits.

First, the ionization process was simulated using the SRIM code [46]. Second, the transport process of generated electrons was simulated with the GARFIELD++ code [47] by using the drift velocity and diffusion coefficient of electrons calculated with the MAGBOLTZ code [48]. Third, the gas amplification process of the electrons reached the GEM, and μ-PIC was calculated with a simple stochastic model in which the amplification factor was assumed to be a random variable according to the Pólya distribution. Finally, the pseudodata set (hit pattern and signal shape) was virtually produced by a software that emulated the readout circuit [49]. The parameters for this simulation were optimized to reproduce the real data taken in the experiment.

The detection efficiency was estimated by analyzing the simulated pseudodata. We defined the detection efficiency as the survival ratio of the produced events after the analysis. We evaluated the efficiency at every polar and azimuthal angular bin with steps of $\Delta\theta = \Delta\phi = 20°$ and at energy bins with a step of $\Delta E_\gamma = 500$ keV over $E_\gamma = 19$–30 MeV.

C. Beam analysis

The energy profile and total photon number of the beams irradiated on the MAIKo active target were estimated from the energy spectrum measured with the beam monitor located at the most downstream of the beam line. A NaI(Tl) scintillation detector was employed as the beam monitor.

The energy profile was estimated from a Monte Carlo simulation of the LCS beam generation process. We generated LCS photons at the collision point using realistic values of the parameters for the electron beam and the laser optical system, such as beam emittance and beam size. We also virtually transported the LCS photons toward the NaI(Tl) beam monitor in the experimental hutch. The interactions of the LCS photons with the beam-line materials were simulated by using the GEANT4 toolkit [50]. The incident energy spectrum of the LCS photons estimated by the simulation is shown in Fig. 4(a). Its deduced energy-deposit spectrum folded with the finite energy resolution of the NaI(Tl) detector was compared with the experimental spectrum measured when the beam intensity was as low as several thousands photons per second in Fig. 4(b).

Figure 5(a) shows a typical energy spectrum measured with the beam monitor when the maximum LCS-photon energy was 30.0 MeV, and the beam intensity was approximately 172 k photons per second. Notably, several discrete peak structures were observed. These structures were due to the multihit events in which multiple LCS photons were detected simultaneously. The LCS photons intermittently arrived at the beam monitor at 16 kHz, which was synchronized with the repetition frequency of the laser module for the LCS photon production. In a single beam pulse, the number of photons varied between one and a few tens. Because the time difference among the LCS photons in one pulse was shorter than the time resolution of the beam monitor, these photons were detected as a single signal. The discrete peaks in the spectrum correspond to one, two, three, and more photons in the order from left. This distribution can be resolved as a
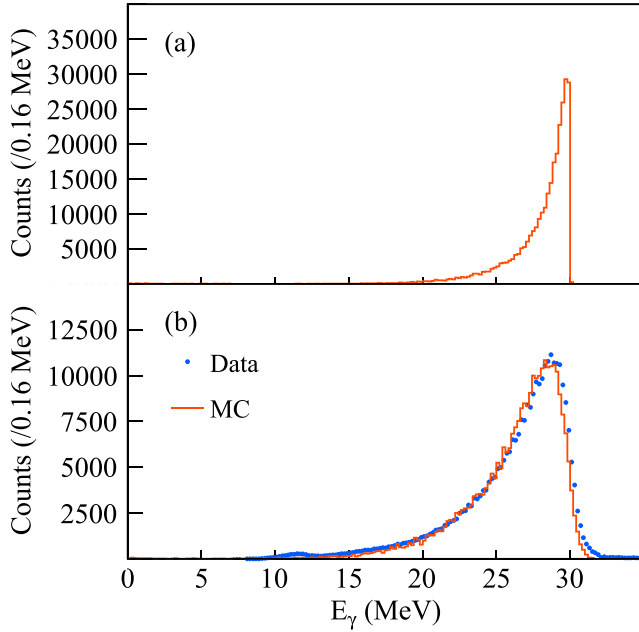
FIG. 4. (a) Energy spectrum of the LCS photons estimated by the Monte Carlo simulation when the maximum LCS-photon energy is 30.0 MeV. (b) Simulated energy spectrum measured by the NaI(Tl) beam monitor compared with the experimental spectrum. The red solid line shows the simulated spectrum whereas the blue solid circles show the experimental spectrum.
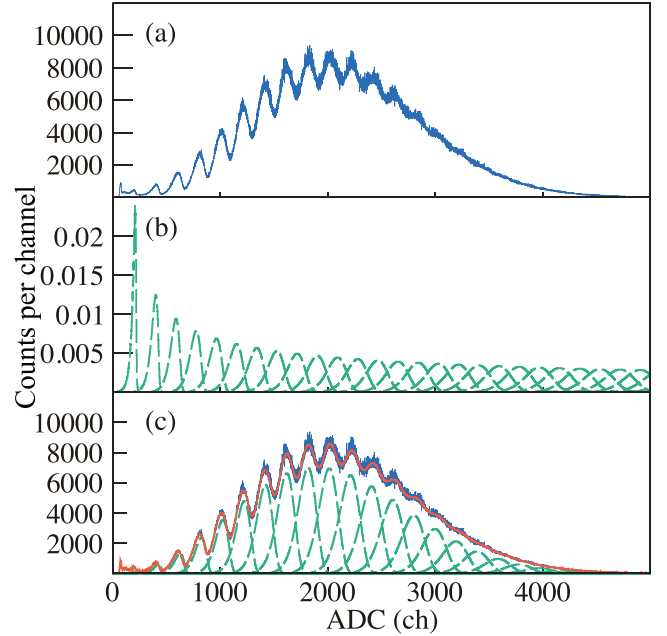

FIG. 5. Typical procedure for estimating the LCS-photon number. (a) Energy spectrum measured with the NaI(Tl) beam monitor. (b) Response functions of the NaI(Tl) beam monitor for various photon multiplicities. (c) Best fit result (thick red solid line) to the measured spectrum (blue solid line) by the response functions multiplied by the weight factors (green dashed line). The quenching effect of the signals induced on the NaI(Tl) scintillator was taken into account (see text).

linear combination of detector-response functions for various photon multiplicities.

The response function for one photon injection was obtained from the measurement with a low-intensity beam. The multiphoton response templates of up to 60 photons were also generated from the iterative convolutions of the one photon response. Figure 5(b) shows the response functions for various photon multiplicities. These functions are normalized so that the integral values are equal to unity. Moreover, the response function of the background events caused by a source other than the LCS was generated from the measurement with the laser turned off. The counts at the x channel in the measured energy spectrum should be described by the template function $T(x)$ composed of a linear combination of the detector-response functions and the background response as follows:

$$T(x) = \sum_{n=1}^{60} w_n t_n(x) + w_{\mathrm{BG}} t_{\mathrm{BG}}(x), \qquad (1)$$

where $t_n(x)$ and $t_{\mathrm{BG}}(x)$ stand for the i photons and the background response functions, and w_i and w_{BG} are the weighting factors for the response functions. In addition, the quenching effect of the signals induced on the NaI(Tl) scintillator was also taken into account by distorting $T(x)$ using the empirical saturation function described in Ref. [51]. We fitted this function to the measured energy spectra to determine the weighting factors and the parameters for the saturation function reproducing the spectra best. Figure 5(c) shows the best-fit template functions compared with the measured

spectrum. The distorted response functions multiplied by the weight factors are also displayed with green dashed lines.

The total photon number irradiated on the MAIKo active target N_γ was determined as

$$N_\gamma = \sum_{n=1}^{60} n w_n, \qquad (2)$$

by using the weighting factors determined from the fitting. The statistical uncertainty of the total photon number was estimated to be approximately 0.2%. The systematic uncertainty originated from the fitting procedure, the quenching of detector output, the contribution from the background events, and the photon multiplicity higher than 60 was approximately 4%.

D. Cross sections

Energy averaged total cross sections of the photodisintegrations were determined from the yield (Y), the detection efficiency (ϵ), and total photon number (N_γ). Here, we define the energy-profile function $f_k(E)$, where k is the index of the beam energy listed in Table I. The energy-profile function $f_k(E)$ was estimated by the Monte Carlo simulation described in Sec. III C [see Fig. 4(a)] and normalized so that the energy-integral value was equal to the total photon number $N_{\gamma,k}$ as

$$N_{\gamma,k} = \int_0^{E_{\mathrm{max},k}} dE f_k(E), \qquad (3)$$

where $E_{\max,k}$ denotes the maximum energy of the photon beam.

In preparation for determining the total cross sections, we first evaluated the differential cross section at each angular bin using the following formula:

$$\left\langle \frac{d\sigma}{d\Omega} \right\rangle_{\theta_i,\phi_j,k} = \frac{Y_{i,j,k}}{\left[\int_0^{E_{\max,k}} dE\, f_k(E)\epsilon_{i,j,k}(E) \right] \tau\, \Delta\Omega_{i,j}}, \quad (4)$$

where i and j are the indices of the angular bins of θ and ϕ whereas k is the index of the beam energy. Here, τ is the target thickness given in the areal number density of ^{4}He nuclei, and $\Delta\Omega_{i,j}$ is the solid angle of the angular bin with $\Delta\phi = \Delta\theta = 20°$ around θ_i and ϕ_j, respectively.

The total cross section is obtained by integrating the differential cross sections over the full solid angle of 4π. In the present analysis, however, the cross sections in the angular bins with lower detection efficiencies must be removed from the integration because those angular bins caused larger systematic uncertainties amplified by the efficiencies. Hereafter, we define $\Delta\tilde{\Omega}_k$ as the angular range in which the differential cross sections are reliable and included in the analysis.

In order to obtain the total cross section, it is necessary to deduce the correction factor for converting the cross section integrated over the partial solid angle $\Delta\tilde{\Omega}_k$ into that over 4π. For this purpose, we assume the photodisintegration reactions in the present energy region are primarily induced through the $E1$ transition, and model the angular distribution of the differential cross sections at $E_\gamma = E$ by the following formula:

$$\left(\frac{d\sigma_M}{d\Omega} \right)_k = \sigma_M(E) \left\{ \frac{3}{8\pi} \sin^2\theta [1 + \alpha_k \cos 2(\phi - \tilde{\phi})] \right\}, \quad (5)$$

where θ and ϕ are the polar and azimuthal angles of the decay particles in the center of mass frame. $\tilde{\phi}$ and α_k are the polarization direction of the linearly polarized photon beam and the azimuthal asymmetry parameter, respectively. σ_M corresponds to the total cross section obtained by integrating the modeled differential cross section over 4π. In addition, we assume that the energy dependence of the modeled total cross section $\sigma_M(E)$ is given by

$$\sigma_M(E) = \begin{cases} \sum_{l=1}^4 p_l (E - E_{\mathrm{th}})^l & (E \geqslant E_{\mathrm{th}}) \\ 0 & (E < E_{\mathrm{th}}), \end{cases} \quad (6)$$

where E_{th} is the threshold energy of the photodisintegration reactions.

Based on the cross section model described above, the expected yield $\tilde{Y}$ at a certain angular bin is estimated as

$$\tilde{Y}_{\theta_i,\phi_j,k} = \tau \int d\Omega \int_0^{E_{\max,k}} dE \left[I_{\Delta\Omega_{i,j}} \left(\frac{d\sigma_M}{d\Omega} \right)_k f_k \epsilon_{i,j,k} \right]. \quad (7)$$

Here, for the sake of simplicity, the arguments (E, θ, and ϕ) of the functions in the integrand are omitted. I_A is an indicator function on the angular range which is defined as

$$I_A(x) = \begin{cases} 1 & (x \in A) \\ 0 & (x \notin A). \end{cases} \quad (8)$$

Therefore, the angular integration in Eq. (7) was done within an angular bin $\Delta\Omega_{i,j}$ with $\Delta\phi = \Delta\theta = 20°$ around θ_i and ϕ_j. This angular bin is the same as that employed in Eq. (4). The unknown parameters, α_k and p_l in Eqs. (5) and (6), were optimized to maximize the likelihood of the expected yields $\tilde{Y}$ by comparing them with the measured yields Y at all angular bins and beam energies while $\tilde{\phi}$ was fixed at $\tilde{\phi} = 10°$.

The average beam energy $\langle E \rangle_k$ was calculated from the weighted mean of the beam energy defined as follows:

$$\langle E \rangle_k = \frac{\int_0^{E_{\max,k}} dE \int d\Omega \left\{ E \left[I_{\Delta\tilde{\Omega}_k} \left(\frac{d\sigma_M}{d\Omega} \right)_k f_k \epsilon_{i,j,k} \right] \right\}}{\int_0^{E_{\max,k}} dE \int d\Omega \left[I_{\Delta\tilde{\Omega}_k} \left(\frac{d\sigma_M}{d\Omega} \right)_k f_k \epsilon_{i,j,k} \right]}. \quad (9)$$

Finally, the measured cross sections were corrected to obtain the experimental total cross section at the average beam energy $\langle E \rangle_k$ by the formula

$$\langle \sigma \rangle_k = C_k \langle \sigma \rangle_{\Delta\tilde{\Omega}_k} \quad (10)$$

$$= C_k \sum_{\theta_i,\phi_j}^{\Delta\tilde{\Omega}_k} \left\langle \frac{d\sigma}{d\Omega} \right\rangle_{\theta_i,\phi_j,k} \Delta\Omega_{i,j}, \quad (11)$$

where the correction factor C_k is given as

$$C_k = \frac{\sigma_M(\langle E \rangle_k)}{\int d\Omega \left[I_{\Delta\tilde{\Omega}_k} \left(\frac{d\sigma_M}{d\Omega} \right)_k (\langle E \rangle_k) \right]}. \quad (12)$$

The second factor in Eq. (10), $\langle \sigma \rangle_{\Delta\tilde{\Omega}_k}$ is the integration of the differential cross section in Eq. (4) over the angular bins adopted in the analysis. The correction factor C_k corresponds to the ratio of the modeled cross section integrated over 4π to that over $\Delta\tilde{\Omega}_k$. The uncertainty of the total cross sections due to the assumption on the angular distribution of the differential cross section was evaluated by using a general formula given in Ref. [32] instead of Eq. (5), and that due to the definition of $\Delta\tilde{\Omega}_k$ was also estimated by varying $\Delta\tilde{\Omega}_k$. They were included in the systematic uncertainty of the total cross sections.

IV. RESULTS AND DISCUSSION

The total cross section of the ^{4}He$(\gamma, n)\,^3$He and ^{4}He$(\gamma, p)\,^3$H reactions measured in the present work are given in Table II and plotted using the upward triangles in Fig. 6. The statistical and systematic uncertainties are shown as the bars and the bands, respectively.

The systematic uncertainties considered in the present study are summarized below. The uncertainty, which is primarily due to the correction of the solid angle and the model selection, is estimated to be varying between ten and a few tens of percentages, depending on the measurement conditions. In addition, the uncertainty from the efficiency estimations due to the incompleteness of the Monte Carlo simulations was approximately 10%, which is taken from Ref. [52]. As discussed in Sec. III C, the uncertainty of the incident photon number was 4%. We monitored and controlled the density of the target gas, and uncertainty originated from that was 0.1% or less.

TABLE II. Experimental total cross sections for the ^{4}He$(\gamma, n)\,^3$He and ^{4}He$(\gamma, p)\,^3$H reactions. The average beam energies $\langle E \rangle_k$ obtained from Eq. (9) and the statistical and systematic uncertainties are also presented. k is an index of beam energy defined in Table I.

| | | ^{4}He$(\gamma, n)\,^3$He | | | | ^{4}He$(\gamma, p)\,^3$H | | | |
| | $E_{\max}$ | $\langle E \rangle_k$ | $\langle \sigma \rangle_k$ | $\Delta\sigma_{stat}$ | $\Delta\sigma_{sys}$ | $\langle E \rangle_k$ | $\langle \sigma \rangle_k$ | $\Delta\sigma_{stat}$ | $\Delta\sigma_{sys}$ |
k	(MeV)	(MeV)	(mb)	(mb)	(mb)	(MeV)	(mb)	(mb)	(mb)
1	23.0	22.5	1.15	± 0.08	$+0.13-0.13$	22.5	1.25	± 0.08	$+0.56-0.40$
2	24.0	23.5	1.31	± 0.10	$+0.14-0.15$	23.3	1.41	± 0.07	$+0.28-0.28$
3	25.0	24.5	1.66	± 0.12	$+0.18-0.18$	24.3	1.64	± 0.08	$+0.25-0.22$
4	27.0	26.5	2.26	± 0.25	$+0.25-0.24$	25.7	1.93	± 0.13	$+0.34-0.42$
5	28.0	27.5	1.94	± 0.19	$+0.21-0.24$	26.5	1.59	± 0.09	$+0.63-0.21$
6	30.0	29.4	1.26	± 0.11	$+0.16-0.19$	28.7	1.67	± 0.05	$+0.19-0.23$

The experimental total cross sections measured with the quasi-monoenergetic photon beams [32,33,36,37] were selected from numerous previous studies and compared with the present results in Fig. 6. The present results showing the GDR peak structure around $E_\gamma = 26$ MeV in both the ^{4}He$(\gamma, n)\,^3$He and ^{4}He$(\gamma, p)\,^3$H reactions do not support those reported by Shima *et al.* [32], but are consistent with those from the HIγS group [36,37]. The uncertainties in the present results are slightly higher than those in previous studies, but smaller than the difference between the results by Shima *et al.* and those by the HiγS group. Notably, the present ^{4}He$(\gamma, n)\,^3$He result also agrees with that by the MAX-lab group [33], which was obtained by using energy-tagged

bremsstrahlung photons. The GDR peak energy is in accord with the theoretical calculation [39] shown by the solid lines in Fig. 6. In addition, the absolute values of our data support the theoretical calculations within the uncertainty except for some points of the ^{4}He$(\gamma, n)\,^3$He reaction whereby their statistical uncertainties are higher than those of others.

As described in Sec. I, the cross sections of the ^{4}He photodisintegration reactions in the GDR energy region are important to elucidate the certain processes in the nucleosynthesis in the universe. Because cross sections theoretically calculated from the nuclear structure theory are generally employed for the astrophysical calculation, one would have to revise the theoretical frameworks and the scenario of the nucleosynthesis if the theoretical predictions largely deviate from the experimental cross sections. The striking experimental results reported by Shima *et al.* challenged the conventional view of the ^{4}He photodisintegration reactions that the GDR peak was located around $E_\gamma = 26$ MeV. However, the present results support the conventional view and do not force one to revise the physical pictures on the nucleosynthesis drawn by the nuclear structure theories.

FIG. 6. Experimental cross sections of the (a) ^{4}He$(\gamma, n)\,^3$He and (b) ^{4}He$(\gamma, p)\,^3$H reactions. The present result (upward triangles) is compared with those from previous studies ([32]: circles, [33]: downward triangles, [36] and [37]: squares). Systematic uncertainties of the cross sections are indicated with hatched regions. The theoretical predictions taken from Ref. [39] are shown by the solid lines.

V. SUMMARY

We performed a simultaneous measurement of the ^{4}He$(\gamma, n)\,^3$He and ^{4}He$(\gamma, p)\,^3$H reactions at the BL01 in the New-SUBARU synchrotron radiation facility by using the TPC-based gaseous active target, MAIKo. Quasi-monoenergetic photon beams at $E_\gamma = 23$–30 MeV, which were close to the GDR energy in ^{4}He, were irradiated on the MAIKo active target. Three-dimensional trajectories of charged particles emitted from the photonuclear reactions were measured, and the ^{4}He photodisintegration events were identified. The detection efficiencies of the photodisintegration events by the MAIKo active target were estimated with the Monte Carlo simulation in which the response of the detector was considered. The total photon number and energy distribution of photon beams were evaluated from the energy spectra measured with the NaI(Tl) scintillator. Finally, we determined the cross sections of the ^{4}He$(\gamma, n)\,^3$He and ^{4}He$(\gamma, p)\,^3$H reactions.

The cross sections obtained from the present measurement show the GDR peaks around $E_\gamma = 26$ MeV. This result is in accord with the experimental results from the HIγS facility
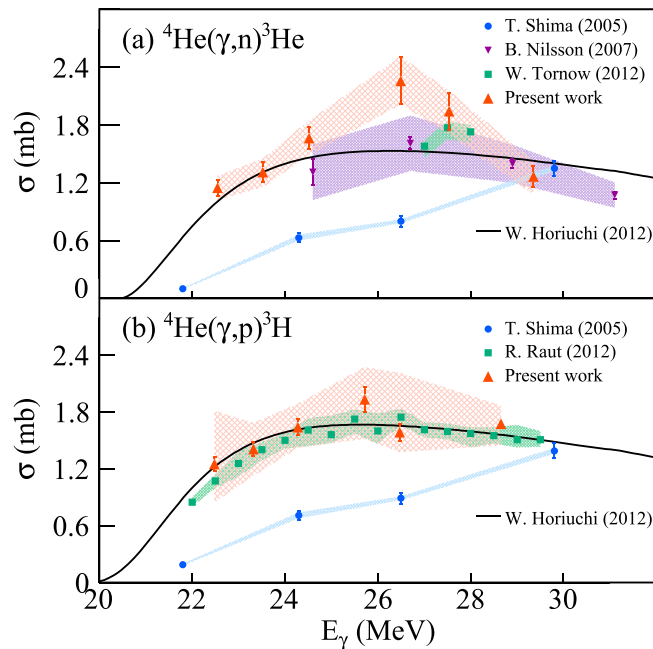
[36,37] and the MAX-lab facility [33] but inconsistent with the result from Shima *et al.* [32]. The present results support the theoretical predictions for the ^{4}He photodisintegration reactions [38,39], and do not force one to revise the theoretical frameworks.

This study demonstrated the applicability of the MAIKo active target, which was originally designed for the in-beam spectroscopy of the unstable nuclei [43], to the study of the photonuclear reactions. The present work expanded our capability of providing reliable data on important reactions in nuclear astrophysics with the MAIKo active target.

[1] A. Bohr and B. Mottelson, *Nuclear Structure II* (Benjamin, Reading, MA, 1975).

[2] S. E. Woosley, D. H. Hartmann, R. D. Hoffman, and W. C. Haxton, The ν-process, Astrophys. J. **356**, 272 (1990).

[3] T. Suzuki and T. Kajino, Element synthesis in the supernova environment and neutrino oscillations, J. Phys. G: Nucl. Part. Phys. **40**, 083101 (2013).

[4] S. X. Nakamura, H. Kamano, Y. Hayato, M. Hirai, W. Horiuchi, S. Kumano, T. Murata, K. Saito, M. Sakuda, T. Sato, and Y. Suzuki, Towards a unified model of neutrino-nucleus reactions for neutrino oscillation experiments, Rep. Prog. Phys. **80**, 056301 (2017).

[5] H. Ejiri, A. I. Titov, M. Boswell, and A. Young, Neutrino-nuclear response and photonuclear reactions, Phys. Rev. C **88**, 054610 (2013).

[6] M. Kusakabe, T. Kajino, T. Yoshida, T. Shima, Y. Nagai, and T. Kii, New constraints on radiative decay of long-lived particles in big bang nucleosynthesis with new ^{4}He photodisintegration data, Phys. Rev. D **79**, 123513 (2009).

[7] S. G. Ryan, T. C. Beers, K. A. Olive, B. D. Fields, and J. E. Norris, Primordial lithium and big bang nucleosynthesis, Astrophys. J. Lett. **530**, L57 (2000).

[8] J. Meléndez and I. Ramírez, Reappraising the spite lithium plateau: Extremely thin and marginally consistent with WMAP data, Astrophys. J. Lett. **615**, L33 (2004).

[9] M. Asplund, D. L. Lambert, P. E. Nissen, F. Primas, and V. V. Smith, Lithium isotopic abundances in metal-poor halo stars, Astrophys. J. **644**, 229 (2006).

[10] A. N. Gorbunov and V. M. Spiridonov, Photodisintegration of helium. I, Zh. Eksp. Teor. Fiz. **33**, 21 (1957) [Sov. Phys. JETP **6**, 16 (1958)].

[11] A. N. Gorbunov and V. M. Spiridonov, Photodisintegration of helium. II, Zh. Eksp. Teor. Fiz. **34**, 862 (1958) [Sov. Phys. JETP **7**, 596 (1958)].

[12] C. C. Gardner and J. D. Anderson, Gamma yield from the proton bombardment of tritium, Phys. Rev. **125**, 626 (1962).

[13] D. Gemmell and G. Jones, The T(p, γ)He^4 reaction, Nucl. Phys. **33**, 102 (1962).

[14] H. Clerc, R. Stewart, and R. Morrison, Photodisintegration of ^{4}He, Phys. Lett. **18**, 316 (1965).

[15] A. Gorbunov, Study of the ^{4}He (γ, p) ^{3}H and ^{4}He(γ, n) ^{3}He reactions, Phys. Lett. B **27**, 436 (1968).

[16] W. E. Meyerhof, M. Suffert, and W. Feldman, ^{3}H(p, γ) ^{4}He reaction from 3 to 18 MeV, Nucl. Phys. A **148**, 211 (1970).

[17] J. Sanada, M. Yamanouchi, N. Sakai, and S. Seki, Study of the excited states in ^{4}He through the ^{4}He(γ, p) ^{3}H reaction, J. Phys. Soc. Jpn. **28**, 537 (1970).

[18] B. Berman, F. Firk, and C.-P. Wu, The 90° differential cross section for the reaction ^{4}He (γ, n_0) ^{3}He and evidence for isospin mixing in the dipole states of ^{4}He, Nucl. Phys. A **179**, 791 (1972).

[19] J. D. Irish, R. G. Johnson, B. L. Berman, B. J. Thomas, K. G. McNeill, and J. W. Jury, 90° differential cross section for the reaction ^{4}He(γ, n) ^{3}He, Phys. Rev. C **8**, 1211 (1973).

[20] C. Malcom, D. Webb, Y. Shin, and D. Skopik, Evidence of a 2^+ state from the ^{4}He(γ, n) ^{3}He reaction, Phys. Lett. B **47**, 433 (1973).

[21] Yu. M. Arkatov, P. I. Vatset, V. I. Voloshchuk, V. A. Zolenko, I. M. Prokhorets, and V. I. Chmil, Energy moments of the total γ-quanta absorption cross section for ^{4}He nucleus, Yad. Fiz. **19**, 1172 (1974) [Sov. J. Nucl. Phys. **19**, 598 (1974)].

[22] F. Balestra, E. Bollini, L. Busso, R. Garfagnini, C. Guaraldo, G. Piragino, R. Scrimaglio, and A. Zanini, Photodisintegration of ^{4}He in the giant-resonance region, Nuovo Cimento A **38**, 145 (1977).

[23] B. L. Berman, D. D. Faul, P. Meyer, and D. L. Olson, Photoneutron cross section for ^{4}He, Phys. Rev. C **22**, 2273 (1980).

[24] L. Ward, D. R. Tilley, D. M. Skopik, N. R. Roberson, and H. R. Weller, Confirmation of the photoneutron cross section for ^{4}He below 33 MeV, Phys. Rev. C **24**, 317 (1981).

[25] R. C. McBroom, H. R. Weller, N. R. Roberson, and D. R. Tilley, ^{3}H(p, γ) ^{4}He reaction below $E_p = 30$ MeV, Phys. Rev. C **25**, 1644 (1982).

[26] J. R. Calarco, S. S. Hanna, C. C. Chang, E. M. Diener, E. Kuhlmann, and G. A. Fisher, Absolute cross section for the reaction ^{3}H(p, γ_0) ^{4}He and a review of ^{4}He(γ, p_0) ^{3}H measurements, Phys. Rev. C **28**, 483 (1983).

[27] R. Bernabei, A. Chisholm, S. d'Angelo, M. P. De Pascale, P. Picozza, C. Schaerf, P. Belli, L. Casano, A. Incicchitti, D. Prosperi, and B. Girolami, Measurement of the ^{4}He$(\gamma, p)^3$ H total cross section and charge symmetry, Phys. Rev. C **38**, 1990 (1988).

[28] G. Feldman, M. J. Balbes, L. H. Kramer, J. Z. Williams, H. R. Weller, and D. R. Tilley, ^{3}H$(p, \gamma)^4$ He reaction and the $(\gamma, p)/(\gamma, n)$ ratio in ^{4}He, Phys. Rev. C **42**, R1167 (1990).

[29] R. J. Komar, H.-B. Mak, J. R. Leslie, H. C. Evans, E. Bonvin, E. D. Earle, and T. K. Alexander, ^{3}He(n,γ)^4 He cross section and the photodisintegration of ^{4}He, Phys. Rev. C **48**, 2375 (1993).

[30] L. Van Hoorebeke, R. Van de Vyver, V. Fiermans, D. Ryckbosch, C. Van den Abeele, and J. Dias, Direct measurement of the ^{4}He(γ, p_0) absolute cross section, Phys. Rev. C **48**, 2510 (1993).

[31] K. I. Hahn, C. R. Brune, and R. W. Kavanagh, ^{3}H$(p, \gamma)^4$He cross section, Phys. Rev. C **51**, 1624 (1995).

[32] T. Shima, S. Naito, Y. Nagai, T. Baba, K. Tamura, T. Takahashi, T. Kii, H. Ohgaki, and H. Toyokawa, Simultaneous measurement of the photodisintegration of ^{4}He in the giant dipole resonance region, Phys. Rev. C **72**, 044004 (2005).

[33] B. Nilsson, J.-O. Adler, B.-E. Andersson, J. R. M. Annand, I. Akkurt, M. J. Boland, G. I. Crawford, K. G. Fissum, K. Hansen, P. D. Harty, D. G. Ireland, L. Isaksson, M. Karlsson, M. Lundin, J. C. McGeorge, G. J. Miller, H. Ruijter, A. Sandell, B. Schröder, D. A. Sims, and D. Watts (The MAX-lab Nuclear Physics Working Group), Measurement of the ^{4}He(γ, n) reaction from $23 < E_\gamma < 70$ MeV, Phys. Rev. C **75**, 014007 (2007).

[34] S. Nakayama, E. Matsumoto, R. Hayami, K. Fushimi, H. Kawasuso, K. Yasuda, T. Yamagata, H. Akimune, H. Ikemizu, M. Fujiwara, M. Yosoi, K. Nakanishi, K. Kawase, H. Hashimoto, T. Oota, K. Sagara, T. Kudoh, S. Asaji, T. Ishida, M. Tanaka *et al.*, Analog of the giant dipole resonance in ^{4}He, Phys. Rev. C **76**, 021305(R) (2007).

[35] T. Shima, Y. Nagai, S. Miyamoto, S. Amano, K. Horikawa, and T. Mochizuki, New results on photodisintegration of ^{4}He, PoS **CD09**, 107 (2010).

[36] W. Tornow, J. H. Kelley, R. Raut, G. Rusev, A. P. Tonchev, M. W. Ahmed, A. S. Crowell, and S. C. Stave, Photodisintegration cross section of the reaction ^{4}He$(\gamma, n)^3$He at the giant dipole resonance peak, Phys. Rev. C **85**, 061001(R) (2012).

[37] R. Raut, W. Tornow, M. W. Ahmed, A. S. Crowell, J. H. Kelley, G. Rusev, S. C. Stave, and A. P. Tonchev, Photodisintegration Cross Section of the Reaction ^{4}He$(\gamma, p)^3$H between 22 and 30 MeV, Phys. Rev. Lett. **108**, 042502 (2012).

[38] S. Quaglioni, W. Leidemann, G. Orlandini, N. Barnea, and V. D. Efros, Two-body photodisintegration of ^{4}He with full final state interaction, Phys. Rev. C **69**, 044002 (2004).

[39] W. Horiuchi, Y. Suzuki, and K. Arai, *ab initio* study of the photoabsorption of ^{4}He, Phys. Rev. C **85**, 054002 (2012).

[40] S. Miyamoto, Y. Asano, S. Amano, D. Li, K. Imasaki, H. Kinugasa, Y. Shoji, T. Takagi, and T. Mochizuki, Laser Compton back-scattering gamma-ray beamline on newsubaru, Radiat. Meas. **41**, S179 (2006).

[41] H. Utsunomiya, T. Shima, K. Takahisa, D. M. Filipescu, O. Tesileanu, I. Gheorghe, H.-T. Nyhus, T. Renstrm, Y.-W. Lui, Y. Kitagawa, S. Amano, and S. Miyamoto, Energy calibration of the newSUBARU storage ring for laser Compton-scattering gamma rays and applications, IEEE Trans. Nucl. Sci. **61**, 1252 (2014).

[42] A. D'Angelo, O. Bartalini, V. Bellini, P. L. Sandri, D. Moricciani, L. Nicoletti, and A. Zucchiatti, Generation of Compton backscattering γ-ray beams, Nucl. Instrum. Methods Phys. Res. A **455**, 1 (2000).

[43] T. Furuno, T. Kawabata, H. Ong, S. Adachi, Y. Ayyad, T. Baba, Y. Fujikawa, T. Hashimoto, K. Inaba, Y. Ishii, S. Kabuki, H. Kubo, Y. Matsuda, Y. Matsuoka, T. Mizumoto, T. Morimoto, M. Murata, T. Sawano, T. Suzuki, A. Takada *et al.*, Performance test of the MAIKo active target, Nucl. Instrum. Methods Phys. Res. A **908**, 215 (2018).

[44] A. Ochi, T. Nagayoshi, S. Koishi, T. Tanimori, T. Nagae, and M. Nakamura, Development of micro pixel chamber, Nucl. Instrum. Methods Phys. Res. A **478**, 196 (2002).

[45] T. Mizumoto, Y. Matsuoka, Y. Mizumura, T. Tanimori, H. Kubo, A. Takada, S. Iwaki, T. Sawano, K. Nakamura, S. Komura, S. Nakamura, T. Kishimoto, M. Oda, S. Miyamoto, T. Takemura, J. D. Parker, D. Tomono, S. Sonoda, K. Miuchi, and S. Kurosawa, New readout and data-acquisition system in an electron-tracking Compton camera for MeV gamma-ray astronomy (SMILE-II), Nucl. Instrum. Methods Phys. Res. A **800**, 40 (2015).

[46] J. F. Ziegler, M. Ziegler, and J. Biersack, Srim – The stopping and range of ions in matter (2010), Nucl. Instrum. Methods Phys. Res. B **268**, 1818 (2010).

[47] http://garfieldpp.web.cern.ch/garfieldpp/.

[48] S. Biagi, Monte Carlo simulation of electron drift and diffusion in counting gases under the influence of electric and magnetic fields, Nucl. Instrum. Methods Phys. Res. A **421**, 234 (1999).

[49] A. Takada, T. Tanimori, H. Kubo, J. D. Parker, T. Mizumoto, Y. Mizumura, S. Iwaki, T. Sawano, K. Nakamura, K. Taniue, N. Higashi, Y. Matsuoka, S. Komura, Y. Sato, S. Namamura, M. Oda, S. Sonoda, D. Tomono, K. Miuchi, S. Kabuki *et al.*, Simulation of gas avalanche in a micro pixel chamber using Garfield++, J. Instrum. **8**, C10023 (2013).

[50] S. Agostinelli, J. Allison, K. Amako, J. Apostolakis, H. Araujo, P. Arce, M. Asai, D. Axen, S. Banerjee, G. Barrand, F. Behner, L. Bellagamba, J. Boudreau, L. Broglia, A. Brunengo, H. Burkhardt, S. Chauvie, J. Chuma, R. Chytracek, G. Cooperman *et al.*, Geant4—A simulation toolkit, Nucl. Instrum. Methods Phys. Res. A **506**, 250 (2003).

[51] H. Utsunomiya, T. Watanabe, T. Ari-izumi, D. Takenaka, T. Araki, K. Tsuji, I. Gheorghe, D. M. Filipescu, S. Belyshev, K. Stopani, D. Symochko, H. Wang, G. Fan, T. Renstrøm, G. M. Tveten, Y.-W. Lui, K. Sugita, and S. Miyamoto, Photon-flux determination by the poisson-fitting technique with quenching corrections, Nucl. Instrum. Methods Phys. Res. A **896**, 103 (2018).

[52] T. Furuno, T. Kawabata, S. Adachi, Y. Ayyad, Y. Kanada-En'yo, Y. Fujikawa, K. Inaba, M. Murata, H. J. Ong, M. Sferrazza, Y. Takahashi, T. Takeda, I. Tanihata, D. T. Tran, and M. Tsumura, Neutron quadrupole transition strength in ^{10}C deduced from the ^{10}C(α, α') measurement with the MAIKo active target, Phys. Rev. C **100**, 054322 (2019).